Enhanced Plasmonic Biosensors of Hybrid Gold Nanoparticle-Graphene Oxide-Based Label-Free Immunoassay

Nan-Fu Chiu[*] , Chi-Chu Chen, Cheng-Du Yang, Yu-Sheng Kao and Wei-Ren Wu

Abstract

In this study, we propose a modified gold nanoparticle-graphene oxide sheet (AuNP-GO) nanocomposite to detect two different interactions between proteins and hybrid nanocomposites for use in biomedical applications. GO sheets have high bioaffinity, which facilitates the attachment of biomolecules to carboxyl groups and has led to its use in the development of sensing mechanisms. When GO sheets are decorated with AuNPs, they introduce localized surface plasmon resonance (LSPR) in the resonance energy transfer of spectral changes. Our results suggest a promising future for AuNP-GO-based label-free immunoassays to detect disease biomarkers and rapidly diagnose infectious diseases. The results showed the detection of antiBSA in 10 ng/ml of hCG non-specific interfering protein with dynamic responses ranging from 1.45 nM to 145 fM, and a LOD of 145 fM. Considering the wide range of potential applications of GO sheets as a host material for a variety of nanoparticles, the approach developed here may be beneficial for the future integration of nanoparticles with GO nanosheets for blood sensing. The excellent anti-interference characteristics allow for the use of the biosensor in clinical analysis and point-of-care testing (POCT) diagnostics of rapid immunoassay products, and it may also be a potential tool for the measurement of biomarkers in human serum.

Keywords: Gold nanoparticle (AuNP), Graphene oxide sheet (GO), Localized surface plasmon resonance (LSPR), Immunoassays

Background

Carbon molecule-based materials such as carbon nanotubes [1, 2], carbon balls (buckminsterfullerene, C60) [3], two-dimensional graphene [4–6], and graphene oxide (GO) [7–11] have been widely used in biosensors. Among them, the two-dimensional sheet structure of graphene is an ideal material to allow for thin films with high conductivity [12, 13] and excellent optical permeability [14] characteristics and high biocompatibility [15, 16]. For these reasons, graphene-based material is widely use in biomedical and electrochemical sensing technology [17, 18]. In addition, the photoelectric type of biological sensing technology is mainly based on GO [19–21]. Because oxide groups can be adjusted to absorb and radiate a light band gap [22, 23], it is commonly used in fluorescence [24], surface plasmon resonance (SPR) [8–11, 19–21], and localized surface plasmon resonance (LSPR) [25, 26] sensing technology. In particular, GO has unique chemical functional groups (epoxy bridges, hydroxyl groups, pairwise carboxyl groups (carboxyl and carbonyl)) which improve the affinity and covalent bonding of biomolecules.

The synthesis of graphene material combined with nanoparticles (such as Pt, Au, Ag, Pd, and ZnO) has been widely studied for the development of new nanocomposite technology. In particular, the use of gold nanoparticles (AuNPs) has been used as a mechanism for the energy transfer of colorimetric and absorption spectroscopy. In addition, during the last decade, research on AuNPs in visible light has highlighted the unique plasmonic resonance characteristics. Because adjusting the size and shape of AuNPs can change the optical absorption wavelength shift, AuNPs can be used for enhanced plasma absorption and signal amplification

* Correspondence: nfchiu@ntnu.edu.tw
Laboratory of Nano-photonics and Biosensors, Institute of Electro-Optical Science and Technology, National Taiwan Normal University, No. 88, Sec. 4, Ting-Chou Road, Taipei 11677, Taiwan

Chiu et al. Nanoscale Research Letters (2018) 13:152

Page 2 of 11

[27, 28]. Therefore, AuNPs have been extensively used in a wide range of applications such as optoelectronic components because of their special optical and optoelectronic properties to enhance light extraction [29, 30] and light absorption reactions [31–33]. In addition, AuNPs are biocompatible, and they have been studied for their use in chemical sensing, biomedical imaging, cancer therapy [34, 35], drug carrier [32, 33], photothermal therapy [36–38], contrast agent [39], radiosensitizer [40], and biosensing [33, 41–43] applications.

The functionality of the AuNPs was modified by adding the cross linker to avoid oxidation and act as a carrier of phytochemicals or vectors; thus, this combination can increase biocompatibility and bioactivity [44–46]. Cross linkers such as cystamine (Cys) or 8-mercaptooctanoic acid (MOA) are activated by carboxylic acid-terminated thiol self-assembled monolayers (SAMs) on a modified Au surface. MOA binds to the Au surface through the thiol linker (-SH end) resulting in monolayers.

In addition, research on plasmon metal material has also been widely reported. For example, plasmonic metal core shell nanoparticles [47], nanostars [48], and fluorine-doped tin oxide nanoparticles [49] have been shown to enhance the energy band gap, which makes them desirable in solar cell and sensing applications.

Moreover, the use of AuNP-GO hybrids based on chemical synthesis [50–52] and electrostatic self-assembly [53] has been reported in sensor, energy, and catalytic applications. In recent years, an increasing amount of research has focused on the use of AuNP-GO hybrids in biosensors. These hybrids have been shown to be useful in the development of electrochemical [54–59] and surface-enhanced Raman scattering (SERS) [56, 59] platform technology to improve the application in biological assays. However, there are currently no relevant reports on the use of naked eye or colorimetric rapid immunoassay biosensor technology. For example, electrochemical DNA biosensors based on AuNP-GO hybrids have been used to detect breast cancer biomarkers to allow for an early diagnosis. With this biosensor, the detection limit (LOD) of 0.16 nM was obtained with a sensitivity of 378 nA/nM for the ERBB2 biomarker [54]. In addition, an AuNP dotted reduction graphene oxide (rGO-AuNP) nanocomposite-based electrochemical aptasensor has been used to selectively detect a concentration of 3,3′4,4′-polychlorinated biphenyls (PCB77) between 1 pg L^{-1} and 10 μg L^{-1}, with a LOD of 0.1 pg L^{-1} [55]. Moreover, AuNP-GO hybrids have been used as an electrochemical-based biosensor to detect hydrogen peroxide (H$_2$O$_2$), with food dynamic responses ranging from 0.1 to 2.3 mM, and an LOD of 0.01 mM [57]. Another good example is the utilization of AuNP-GO [56, 59] and AuNP-graphene [59] hybrids for SERS-based biosensors in diverse applications, as well as SERS-measured bioimaging.

In this study, we propose an alternative method of chemical synthesis and electrostatic self-assembly of AuNP-GO hybrids using layer-by-layer self-assembly. We also analyze the biological detection sensitivity of the modified combined AuNPs and GO sheets and their protein immune response. We designed two kinds of AuNP-GO-based protein label-free immunoassays and evaluated their response time and sensitivity in antigen-antibody interactions. The excellent sensing features of graphene-AuNP composites include ultra-high sensitivity and the affinity of biomolecule interactions that influence the detection of a diverse range of biomolecules with high specificity. These features imply that these composites have a promising role in future applications, and the potential to be the preferred route of disease detection in clinical diagnosis applications.

Methods/Experimental

Materials

Graphite was purchased from Graphene Supermarket (Graphene Laboratories Inc., Reading, MA, USA). GO sheets were obtained from graphite flakes by using a modified Hummer's method [60] followed by ultrasonic shattering for 5 h for a flake size of 0.1–1 μm and thickness of 1.1 nm. Cystamine dihydrochloride (Cys, 96%), hydrogen tetrachloroaurate(III) trihydrate (HAuCl$_4$·3H$_2$O) , ACS, 99.99% (metals basis), and Au 49.5% min were purchased from Alfa Aesar Co. (USA). Sodium citrate (HOC(COONa)(CH$_2$COONa)$_2$·2H$_2$O) was purchased from J.T. Baker Chemical Co. (USA). Bovine serum albumin (BSA, SI-B4287, Sigma-Aldrich, USA), Anti-Bovine Albumin antibody produced in rabbit (antiBSA, SI-B1520, Sigma-Aldrich, USA), N-hydroxysuccinimide (NHS), and 1-ethyl-3-(3-dimethylaminopropyl)carbodiimide (EDC) were purchased from Sigma-Aldrich Inc. (USA). The immunoglobulins (Ig) of antiBSA antibody structure were produced by B lymphocytes and secreted into the plasma. The monomeric forms of Ig molecules were glycoproteins with a molecular weight of about 150 kDa. Each Ig monomer was capable of binding two antigen molecules. All reagents and solvents were used without further purification.

We used three different temperature conditions at 550, 400, and 100 °C with boiling times of 5, 5, and 120 minutes, respectively, to control reduction of the nanoparticles. These different temperatures reduced the nanoparticles to obtain the same absorption spectrum at 520 nm as clearly seen in Additional file 1: Figure S1.

Synthesis of AuNPs

The method used to obtain AuNPs was based on the use of sodium citrate as a reducing agent to reduce tetrachloroaurate taurine ions in water. A volume of 15 mL of HAuCl$_4$·3H$_2$O solution containing 1 mM of Au was

Chiu *et al. Nanoscale Research Letters* (2018) 13:152

Page 3 of 11

refluxed, and 1.8 mL of 38.8 mM sodium citrate (Na_3
$C_6H_5O_7$) solution was added to the boiling (550 °C, 1100 rpm) solution. The reduction of the gold ions by the citrate ions was complete after 5 min, and the solution was further boiled for 30 min (400 °C, 900 rpm) and then left to cool to room temperature [36, 61, 62]. This method yields spherical AuNPs with an average diameter of about 15 nm, and a reduced concentration of 0.8 mL of 38.8 mM sodium citrate can be used to produce AuNPs with an average diameter of about 60 nm [63, 64]. The chemical reaction is as follows:
$HAuCl_{4(aq)} + C_6H_5O_7Na_{3(aq)} \rightarrow Au_{(s)} + CO_2 + HCOOH$.

Preparation of GO Based on an Antigen Target
We designed an immunoassay method to prepare GO sheets as shown in Fig. 1. We used a 200-μL GO sheet solution at a concentration of 0.1 g/l, and the activation of carboxyl end groups on the surface of GO sheets for covalent bond formation to immobilize hydrocarbon chains was performed using a mixture of 400 μM (EDC)/100 μM (NHS) at a volume ratio of 1:1. The BSA protein was immobilized onto the ends of GO sheets using EDC/NHS to activate and promote covalent bonding reactions between carboxyl groups on GO and –HN_2 of BSA. The activated –COOH surface was then subjected to strong covalent immobilization via an amine (NH_2)-coupling reaction with 20 μl of BSA protein at a concentration of 100 μg/ml. Finally, we used a centrifuge to repeatedly remove non-immobilized BSA protein on the GO surface. The GO-BSA antigen target procedure is shown in Fig. 1.

Preparation of AuNPs and AuNP-GO Based on an Antibody Probe
We performed surface functionalization using Cys with 15-nm AuNPs in a volume of 200 μL. The AuNPs were chemically modified using a derivatized thiol self-assembled monolayer of Cys. The AuNPs were immersed in a solution of Cys (10 mM) for 2 h at room temperature. Because of the strong AuNP–S bond (thiol bond), Cys can easily connect to AuNPs and –NH_2 groups exposed on the surface of AuNPs–Cys–NH_2. We

then added 20 μl of antibodies (antiBSA) of 100 μg/ml protein to immobilize the surface of the AuNPs, followed by repeated centrifugation to remove non-immobilized Cys on the surface of the AuNPs. Deionized water was then used to remove any non-immobilized AuNPs (Cys is an amino thiol structure that does not need to be activated by EDC/NHS). The Cys attached to the AuNPs had amine (–NH_2) groups covalently coupled with carboxyl (–COOH) groups on the surface of anti-BSA. Finally, we used repeated centrifugation to remove non-immobilized antiBSA protein from the surface of the AuNPs. A series of antiBSA protein concentrations were prepared by serial dilution from 100 μg/ml to 1 pg/ml. The preparation of the AuNP-antiBSA probe at different concentrations of antibodies is shown in Fig. 2a.

We used AuNPs prepared using the GO sheet method to modify the AuNP-GO nanocomposite. The AuNPs were prepared using the sodium citrate reduction method, and the size of the 60-nm AuNPs was modified using Cys (5 mM). We then used EDC/NHS to activate the –COOH groups on the surface of the GO sheets. The Cys attached to the AuNPs included –NH_2 groups covalently coupled with –COOH groups on the surface of the GO sheets. The AuNPs on the surface of the GO sheets were immobilizing using a Cys linker to promote covalent bonding reactions between the AuNPs and GO. Covalent coupling offers a stable and easy method for bonding surface functionalization on GO sheets. The GO sheets were thoroughly rinsed with deionized water to remove unbonded GO at the AuNP-linker surface. The AuNP-Cys formed a new composite of AuNP-GO, followed by immobilization with different dilution concentrations from 100 μg/ml to 1 pg/ml of antibody (anti-BSA) probe protein to form AuNP-GO-antiBSA, as shown in Fig. 2b.

Characterization of AuNPs and GO Sheets
The dispersion and morphology of AuNP-GO sheets were characterized using a 300-kV field-emission gun transmission electron microscope (FEG-TEM; Tecnai G2F30S-Twin, Philips-FEI, Amsterdam, Netherlands) and a high-resolution transmission electron microscope
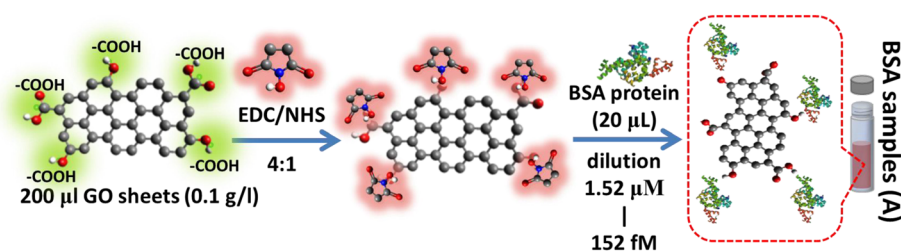

Fig. 1 GO-BSA interaction. The carboxyl group of GO sheets can be activated using EDC/NHS reaction and preparation of the GO based on antigen target for GO-BSA
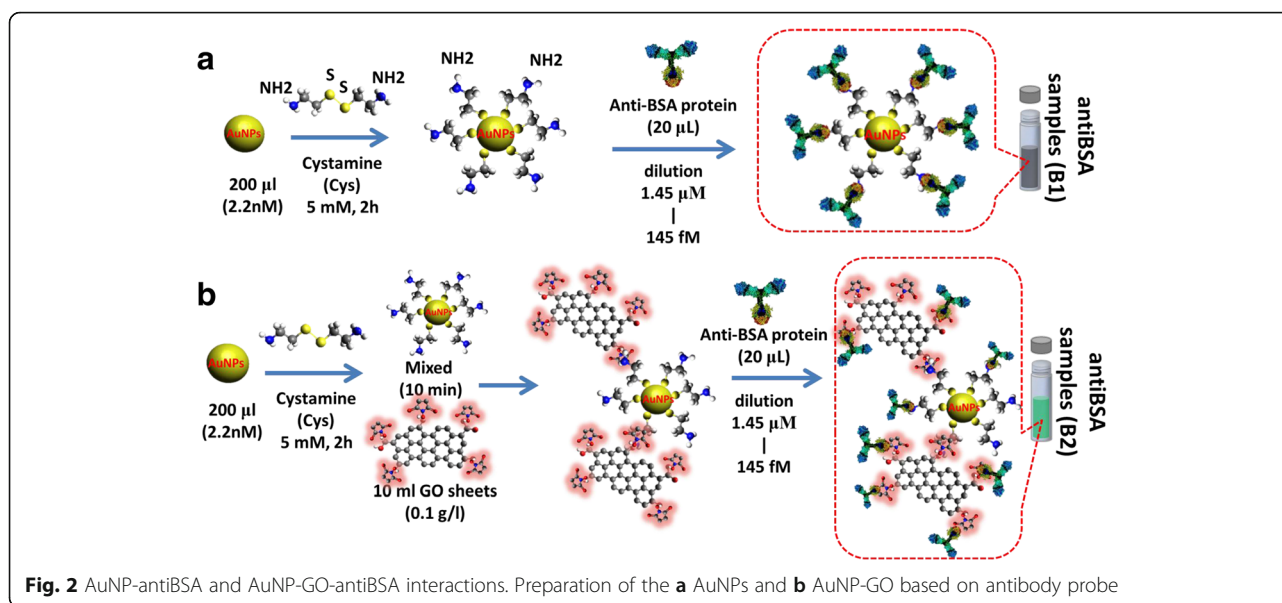
Chiu *et al. Nanoscale Research Letters* (2018) 13:152

Page 4 of 11

Fig. 2 AuNP-antiBSA and AuNP-GO-antiBSA interactions. Preparation of the **a** AuNPs and **b** AuNP-GO based on antibody probe

(HR-TEM) on a FEI Tecnai G20 system (Hillsboro, OR, USA). The dispersion and morphology of the AuNP-GO and GO sheets were characterized using a JEOL JSM-7800F Prime Extreme-resolution Analytical Field Emission Scanning Electron Microscope (JEOL Inc., USA). The ultraviolet-visible (UV-vis) transmittance spectrum of a double beam spectrophotometer was observed using a UV-vis spectrophotometer (U-2900, Hitachi High-Technologies Corporation, Tokyo, Japan) with a wavelength from 200 to 1100 nm at room temperature. Raman measurements were performed using a microscopic Raman system (MRI, Protrustech Co., Ltd., Taiwan). An air-cooled spectrometer (AvaSpec-ULS2048L) with 1800 lines/mm grating and 50-μm slit was used as a detector. Fourier-transform infrared spectrometer (FTIR) measurements were made using a Bruker Vertex 80v spectrometer in attenuated total reflection (ATR) mode, and a DTGS detector (64 scans) with a resolution of 2 cm^{-1} on a KBr pellet in a vacuum at a pressure of around 6 Pa. The Instrumentation Center at National Tsing Hua University provided support for this work. X-ray photoelectron spectroscopy (XPS) was performed using the facilities at the National Synchrotron Radiation Research Center, Hsinchu, Taiwan. The photoelectron spectroscopy experiments were performed using a 09A2 U5-spectroscopy beamline for XPS. Photons with fixed energies of 380 and 900 eV were used for C (1s) and Co (2p) throughout the core-level photoelectron spectroscopy experiments. The experiments were carried out in total-electron-yield mode at a 6-m high-energy spherical grating monochromator. The photons were incident to the normal surface, and photoelectrons were collected at an angle of 58° from the normal surface. The binding energies in all spectra referred to the Au 4f$^{7/2}$ core level at 84.

0 eV. After subtracting the linear background, the spectra were fitted with mixed Gaussian–Lorentzian functions based on a nonlinear least-square algorithm [65].

Results and Discussion

Structure and Morphology Analysis

The size of the AuNPs depended on the nature of the reducing agent and conditions of formation and storage. The SEM analysis indicated that the GO sheets and AuNPs were uniformly attached on the GO surface, with an average AuNP size of 60 nm (Fig. 3). Figure 3a shows SEM images of the GO sheets on the Au film and that the GO sheets were less than 1 μm. Comparing GO and AuNP-GO, a gold element could be observed in the AuNP-GO composite. This indicated that the AuNPs had been successfully adsorbed on the wrinkled GO surface. The synthesized AuNP-GO hybrids were characterized using TEM as shown in Fig. 3b. Figure 3b, c shows the synthesis conditions. The concentration of 10 ml GO sheet solution was 0.1 g/l, and 200 μl of AuNP solution had a concentration of 2.2 nM. The TEM images in Fig. 3a with a 100-nm scale bar and Fig. 3b with a 0.5-μm scale bar show different amplifications of the size and clearly show that the AuNPs were immobilized on the surface of the GO sheets. The AuNPs had a spherical shape, suggesting that carboxylic functionality on the surface of the GO sheets may play an important role in the formation of chemical covalent bonds with the AuNPs as shown in Fig. 2b.

Characterizations of GO by XPS, Raman, and FTIR Spectroscopy

Figure 4a shows the high-resolution C 1s XPS spectral analysis of the GO sheets. The C1s of the highest
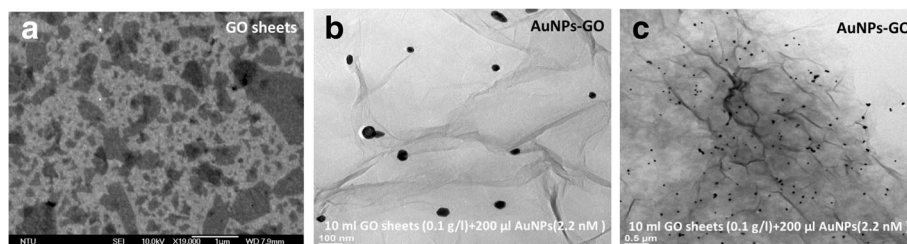
Chiu *et al. Nanoscale Research Letters* (2018) 13:152

Page 5 of 11

Fig. 3 Surface morphology analysis of the nanocomposite. **a** SEM images of a GO sheet and **b** TEM image of AuNP-GO composite. **c** The TEM image of the ERGO AuNP-GO film

intensity at a binding energy of 284.6 eV corresponded to carbonyl functional groups for C–C (sp2), and the peaks at 285.6, 286.6, 288.2, and 289.4 eV corresponded to C–C (sp3) in aromatic rings, C–O in hydroxyl and epoxy groups, C=O in carbonyl groups, and O–C=O in carboxyl groups, respectively. The C 1s XPS spectra of the GO sheets on a gold film substrate showed that the relative atomic percentages of C–C (sp2), C–C (sp3), C–O, C=O, and O–C=O were 77.44, 2.16, 18.14, 1.77, and 0.49%, respectively [66]. Figure 4b shows Raman spectral analysis of the GO sheets in NaCl solution with spectral feature peaks at 1614 cm^{-1} (G band), 1355 cm^{-1} (D band), 2714 cm^{-1} (2D band), 2947 cm^{-1} (G + D band), and ~ 3240 cm^{-1} (2D' band) [38, 67]. The formation of the GO sheets was further analyzed to elucidate the properties of various oxygenated species using ATR-FTIR spectra as shown in Fig. 4c. This ATR-FTIR spectra also revealed several characteristic peaks of GO; C–O at 850 cm^{-1} due to (C–O–C) epoxide vibrations, C–O at 1080 cm^{-1} due to (C–O) alkoxy stretching vibration, C=C at 1500~1600 cm^{-1} due to aromatic C=C bonds, and C–O at 1260 cm^{-1} due to (C–O–C) epoxide asymmetric vibrations. The carboxylic groups at the edges of the GO sheets showed –COOH stretching vibrations, with peaks at 1652 and 1731 cm^{-1} corresponding to C=O stretching vibrations from carbonyl groups. The spectra also showed three peaks at 2900 cm^{-1} related to asymmetric and symmetric stretching vibrations of –CH$_2$ and a deformation peak at 1462 cm^{-1} due to alkene groups (C–H) located on the plane of GO. FTIR spectra of GO showed a large range of absorption broad band peaks of C–OH and H$_2$O vibrations at 3370 cm^{-1} due to stretching vibrations [67].
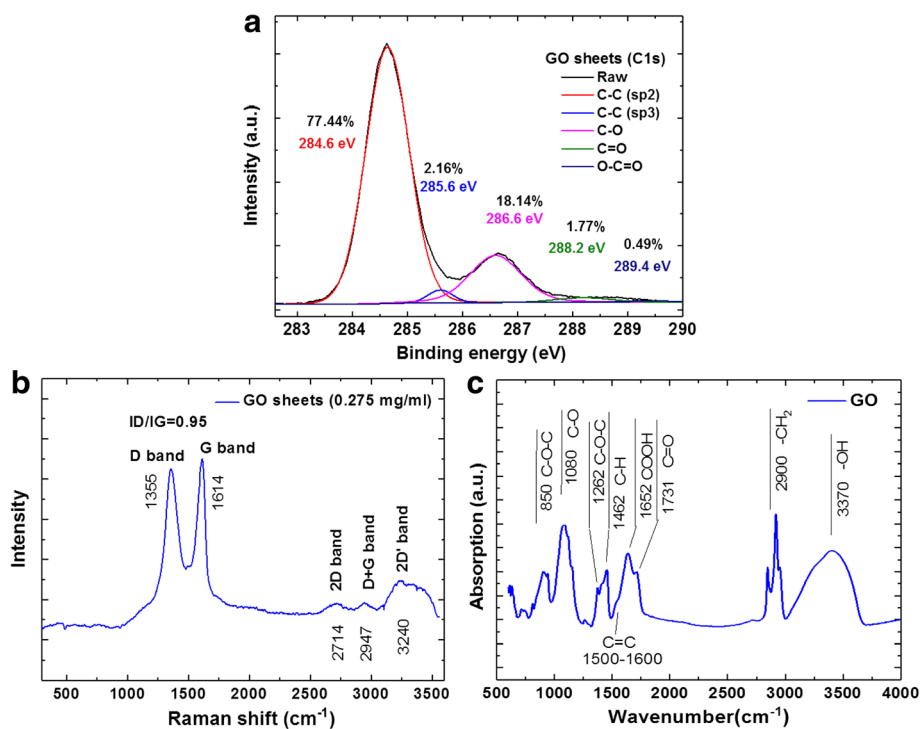

Fig. 4 Spectral analysis of GO sheets. **a** XPS high-resolution scan in the C1s region, **b** Raman, and **c** FTIR

Chiu *et al. Nanoscale Research Letters* (2018) 13:152

Page 6 of 11

Analysis of GO and AuNP with Protein Interaction Properties

UV-vis spectra of aqueous GO and AuNPs with protein interaction dispersions are presented in Fig. 5. The AuNPs had high extinction coefficients and a unique size depending on the surface plasmon (SP) absorption bands. The modified AuNPs of two different dimensions were 15 and 60 nm for 520 and 540 nm of SP absorption spectra [68, 69]. Figure 5a shows the AuNP (520 nm) solution modified with Cys at a concentration of 5 mM with the AuNP-Cys extinction band [69]. The UV-vis spectra of aqueous GO dispersions yielded two absorption peaks: the maximum at 230 nm corresponding to the π–π^* plasmon peak of aromatic C–C bonds in differently sized aromatic sp2 clusters, and the shoulder at 300 nm corresponding to the n–π^* plasmon peak owing to the presence of epoxide and carbonyl (C=O) bonds (Fig. 5b) [9, 20]. The UV-vis spectra of GO–EDC/NHS and GO–EDC/NHS–BSA solution (Fig. 5b) demonstrated that GO–EDC/NHS and GO–EDC/NHS–BSA showed a peak at about 270 nm, which was probably due to strong interactions between GO and amine groups [70, 71]. Figure 5c shows the absorption spectra of the bonds for different concentrations of antiBSA with AuNPs (60 nm). Figure 1b shows the synthesis solution of the AuNP-antiBSA probe (sample B1). The

wavelengths had obvious absorption peaks at 540 and 755 nm, with the wavelength at 540 nm being mainly caused by the AuNPs (60 nm), and the peak at 755 nm corresponding to a AuNP+Cys+antiBSA combination absorption peak. This result showed that an increase in antiBSA concentration induced a gradual increase in the absorbance at 540 nm and a continuous increase in the near-IR absorption at 755 nm. The different antiBSA-binding interactions at the surface of the AuNPs caused changes in the surface refractive index, which in turn was transduced into absorbance intensity of the LSPR. The LSPR band was affected by particle size. The AuNPs showed strong SPR bands in the visible region. With increases in the refractive index of the medium-sized particles, the shift in SPR peak positions could be tuned from the visible to the near-infrared. In the protein interaction experimental results, we mixed AuNP-antiBSA as shown in Fig. 5d. Sensitivity was determined by plotting the LSPR wavelength of the 500–760 nm band as a function of the measured refractive index. We then used dilution different concentrations of antiBSA protein from 1.45 nM to 145 fM and mixed them in a 200-μl volume. The changes in 540 and 760 nm absorption were caused by the different concentrations of antiBSA and AuNP. Spectral measurements were then made 5 min later, which showed different concentrations of
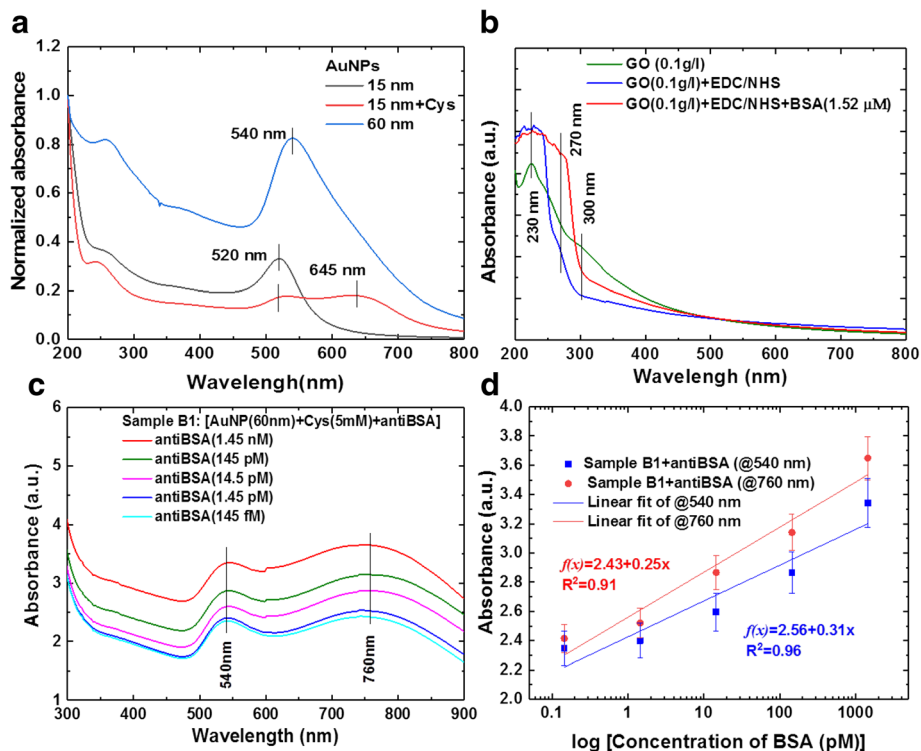

Fig. 5 Analysis of UV-vis absorption spectra for AuNP with antiBSA interaction response. **a** SP absorption spectra of AuNPs, **b** GO-bound BSA, **c** AuNP-anti-BSA probe, and **d** Calibration curves for AuNP with antiBSA interaction response at dilution different concentrations of antiBSA protein from 1.45 nM~145 fM

Chiu *et al. Nanoscale Research Letters* (2018) 13:152

Page 7 of 11

light intensity absorption, and an absorption peak of 60 nm for the AuNPs was observed at 540 and 755 nm. These results were consistent with the AuNP-antiBSA absorption calibration curves. The calibration curves were fitted by $y = 2.43 + 0.25×$ (correlation coefficient, $R^2 = 0.91$) for the 540-nm absorption peak, and $y = 2.56 + 0.31×$ (correlation coefficient, $R^2 = 0.96$) for the 760-nm absorption peak, where x is the concentration of antiBSA and y is the optical absorbance.

Analysis of AuNP-antiBSA and AuNP-GO-antiBSA Based on Immunoassay Interactions

In order to understand the immunological detection mechanism of GO and AuNP-GO nanocomposites, spectral analysis for binding reactions was performed as shown in Fig. 6. Figure 6a shows the UV-vis absorption spectra of the AuNP-GO and GO-BSA nanocomposites. For the GO sheet (0.1 g/l) solution, there was a peak at about 230 nm [70] and a shoulder at around 300 nm, and the GO–BSA conjugates showed an absorption peak at about 270 nm and a peak at about 230 nm [9, 20, 70]. In the combination of AuNP-GO nanocomposites, three absorption peaks were noted at 230, 300, and 540 nm, respectively. The π–π stacking or covalent bonding interactions between AuNPs and the GO sheet surface were the main driving force anchoring the AuNPs onto the highly biocompatible GO materials. The GO sheets

were made to congregate in the AuNPs, resulting in a strong absorption band of 200–300 nm. Therefore, the absorption of the GO sheets was much greater than the absorption of AuNPs in the visible light band. Figure 6b shows that the UV-vis spectra of the AuNP absorption peak were at 540 nm [50, 68, 69]. The absorption peaks were at 540 and 660 nm for AuNP+Cys conjugates; 230, 300, 540, and 660 nm for AuNP+Cys+GO conjugates; and 230, 270, 540 and 660 nm for AuNP+Cys+GO+anti-BSA conjugates. The GO sheets had two absorption peaks at 230 nm (π–π* plasmon peak) and 300 nm (n–π* plasmon peak). A shift in the absorption wavelength was noted, and this absorbance shift was considered to indicate confirmation of antiBSA (0 fM ~ 1. 45 nM) absorption onto the AuNP+Cys+GO surface. Figure 6c shows the synthesis of the solution of the AuNP+Cys+GO+antiBSA probe (sample B2) as in Fig. 2b. The increase in antiBSA concentration was relatively high at 540 nm. Figure 6c shows different concentrations of light intensity absorption, and an absorption peak of 60 nm for the AuNPs was observed at 540 nm. The increase in antiBSA concentration was relatively high at 540 nm. This result showed that AuNP-GO could enhance the plasmon absorption characteristics at 540 nm when the antiBSA concentration was increased. In addition, in the immunoassay experiment, we mixed the GO-BSA (1.52 μM) target (sample A) and AuNP+Cys
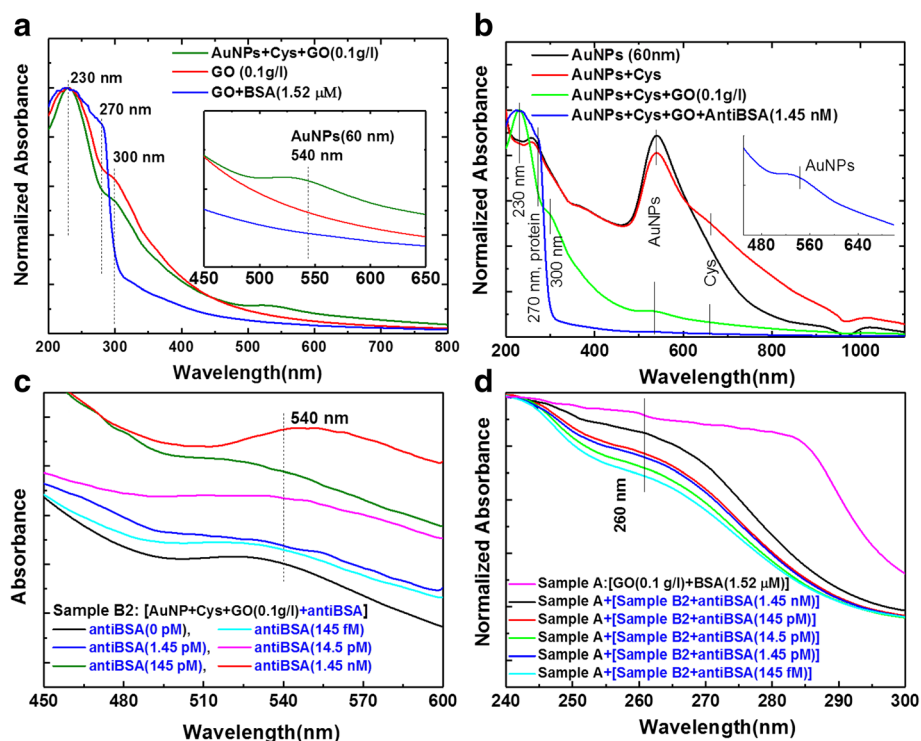

Fig. 6 Analysis of UV-vis absorption spectra for immune response. **a** AuNP-bound GO and GO-bound BSA, **b** AuNPs and GO-bound anti-BSA, **c** AuNP-GO-antiBSA probe, and **d** AuNP-GO-antiBSA probe and GO-BSA target for immune response

Chiu *et al. Nanoscale Research Letters* (2018) 13:152

Page 8 of 11

+GO+antiBSA probe as shown in Fig. 6d. In addition to hydrophobic and π−π interaction characteristics of the GO sheets, covalent bonds between proteins and carboxyl groups on the GO sheets also supported surface adhesion. This result was likely due to the AuNP+GO-antiBSA hybrid structure to form a stable immune response with other proteins on GO-BSA. The wavelengths had an obvious absorption peak at 260 nm. In addition to hydrophobic and π−π (π−π* plasmon peak) interaction characteristics of the GO sheets, covalent bonds between proteins and carboxyl groups on the GO sheets also supported surface adhesion. Before and after BSA and antiBSA bonding, the π−π* plasmon peak values of GO (230 and 270 nm) were significantly shifted, which proved that BSA and antiBSA were positively bonded.

Figure 7 shows that these results were in good agreement with the calibration curves. Detailed analysis of the above experimental results (Fig. 6c, d) showed that the sensing responses to the corresponding average inaccuracies of absorbance were 1.3487, 1.1776, 1.0698, 0.8755, and 0.8588 (Fig. 7a) and 0.9226, 0.8535, 0.7649, 0.7243, and 0.695 (Fig. 7b), corresponding to 1.45 nM, 145 pM, 14.5 pM, 1.45 pM, and 145 fM protein concentrations, respectively. Figure 7a shows that the linear regression of the calibration curves was $f(x) = 0.918 + 0.124\times$ (correlation coefficient, $R^2 = 0.94$) for the AuNP-GO probe with antiBSA interactions, where x is the protein concentration and y is the optical absorbance. In addition, Fig. 7b shows that the linear regression equation of the fitted curve was $f(x) = 0.791 + 0.057\times$ (correlation coefficient, $R^2 = 0.954$) for GO and AuNP-GO based on the immunoassay.

During the quantitation experiment, we added a fixed concentration of 10 ng/ml of human chorionic gonadotropin (hCG) protein to act as an interferer. The results showed that the fixed interferer hCG protein on the immunoassay calibration curves were fitted by $f(x) = 0.843 + 0.113\times$ (correlation coefficient, $R^2 = 0.89$) for the AuNP-GO probe with antiBSA interactions (Fig. 7a), and $f(x) = 0.722 + 0.051\times$ (correlation coefficient, $R^2 = 0.73$) for the GO and AuNP-GO based on the immunoassay (Fig. 7b).

Furthermore, our experimental results showed that the detection strategy allowed for surface regeneration with no loss in specificity (four regenerations) and that it could also be used to detect antiBSA protein with dynamic responses ranging from 1.45 nM, 145 pM, 14.5 pM, 1.45 pM, 145 fM, and 0 fM. The results demonstrated that with a decreased concentration of antiBSA (from 1.45 nM to 145 fM) and even without the presence of antiBSA (0 fM), the spectral absorption intensity did not change the minimum level of quantitation. The hCG protein interfered with the antibody recognition in the immunoassay to a limited extent, possibly due to non-specific adsorption. This implies a very low cross-reactivity of the hCG protein and non-specific interactions at a low adsorption. In the practical quantitative analysis with immunoassays, a LOD of 145 fM for antiBSA was achieved in both buffer and interference protein samples.

Conclusions

We successfully demonstrated a GO-bound AuNP biocompatible nanocomposite in a biosensing mechanism in a rapid and label-free immunoassay for biomolecule interactions. The results showed that the AuNP-GO nanocomposite was biocompatible and exhibited LSPR extinction to biomolecules, which could promote the absorption spectra characteristic peaks, accelerate the reaction of molecules, and enhance the stability of chemical covalent bonds during immobilization. For the detection of antiBSA protein, the limit of detection of the GO and AuNP-GO based on the immunoassay was as low as
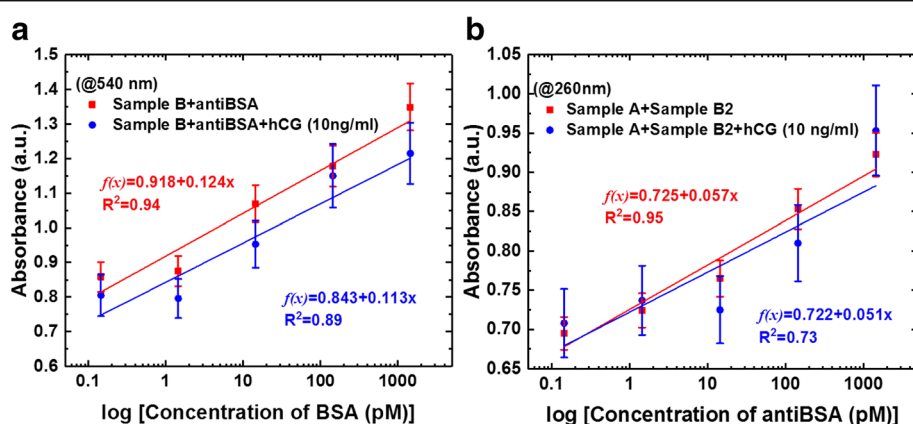

Fig. 7 Comparison of the calibration curves of sensing responses obtained at different protein concentrations. **a** Calibration curves for AuNP-GO probe with antiBSA interactions. **b** Calibration curves for GO and GO-AuNPs based on an immunoassay

Chiu *et al. Nanoscale Research Letters* (2018) 13:152

Page 9 of 11

145 fM. Among the AuNP-GO biosensors, GO immobilized in the AuNP-GO nanocomposite showed the highest bioaffinity, with good sensitivity, low detection limit, and fast response toward the protein immunoassay. The results of our experiments showed that a fixed concentration 10 ng/ml of hCG protein as an interferer did not affect the test response. Given the growing trend of applying biosensors in POCT, LSPR for AuNP-GO nanocomposite technology is a highly promising and versatile tool for use in immunoassays. Combining the properties of AuNPs and GO sheets to develop new nanocomposites for the synthesis of smart materials shows promise for the development of user-friendly diagnosis applications. In the future, AuNP-GO nanocomposites may be used in innovative immunoassays, rapid detection reagents, and miniaturization, which may in turn make LSPR technology an irreplaceable tool for routine clinical analysis and POCT diagnostics.

Additional file

Additional file 1: Figure S1. Comparison of the three different temperatures for the synthesis of AuNPs as shown by the absorption spectrum. (DOCX 43 kb)

Abbreviations
Ag: Silver; AntiBSA: Bovine serum albumin antibody; Au: Gold; AuNP: Gold nanoparticle; BSA: Bovine serum albumin; Cys: Cystamine; EDC: 1-Ethyl-3-(3-dimethylaminopropyl)carbodiimide; FEG-TEM: Field-emission gun transmission electron microscope; FTIR: Fourier-transform infrared spectrometer; GO: Graphene oxide sheet; HR-TEM: High-resolution transmission electron microscope; LOD: Limit of detection; LSPR: Localized surface plasmon resonance; MOA: 8-Mercaptooctanoic acid; NHS: *N*-Hydroxysuccinimide; Pd: Palladium; POCT: Point-of-care testing; Pt: Platinum; RGO: Reduction graphene oxide; SAMs: Self-assembled monolayers; SERS: Surface-enhanced Raman scattering; UV-vis: Ultraviolet-visible; XPS: X-ray photoelectron spectroscopy; ZnO: Zinc oxide

Availability of Data and Materials
All data are fully available without restriction.

Authors' Contributions
All authors contributed to the analysis and discussion of the data and writing the manuscript. N-FC conceived and designed the experiments; C-CC performed the synthesis of AuNP experiments; N-FC, C-CC, and C-DY performed the experiment immunoassay and contributed in data analysis and discussion. C-DY, C-CC, and Y-SK, conducted the XPS, FTIR, TEM, SEM, and Raman of the samples and contributed in data analysis and discussion. W-RW performed the synthesis of the three different temperature (550, 400 and 100 °C) AuNPs samples. N-FC contributed reagents, materials, and analysis tools; N-FC wrote the paper. All authors read and approved the final manuscript.

Authors' Information
Nan-Fu Chiu is an associate professor of Institute of Electro-Optical Science and Technology, National Taiwan Normal University. Chi-Chu Chen is a Master's student of the Institute of Electro-Optical Science and Technology, National Taiwan Normal University. Cheng-Du Yang is a Master's student of the Institute of Electro-Optical Science and Technology, National Taiwan Normal University. Yu-Sheng Kao is a Master's student of the Institute of Electro-Optical Science and Technology, National Taiwan Normal University. Wei-Ren Wu is a Master's student of the Institute of Electro-Optical Science and Technology, National Taiwan Normal University.

Competing Interests
The authors declare that they have no competing interests.

Publisher's Note
Springer Nature remains neutral with regard to jurisdictional claims in published maps and institutional affiliations.

References
1. Angione MD, Pilolli R, Cotrone S, Magliulo M, Mallardi A, Palazzo G, Sabbatini L, Fine D, Dodabalapur A, Cioffi N, Torsi L (2011) Carbon based materials for electronic bio-sensing. Mater Today 14:424–433
2. Rivasa GA, Rubianes MD, Rodríguez MC, Ferreyra NF, Luque GL, Pedano ML, Miscoria SA, Parrado C (2007) Carbon nanotubes for electrochemical biosensing. Talanta 15:291–307
3. Bakry R, Vallant RM, Najam-ul-Haq M, Rainer M, Szabo Z, Huck CW, Bonn GK (2007) Medicinal applications of fullerenes. Int J Nanomedicine 2:639–649
4. Pumera M (2011) Graphene in biosensing. Mater Today 14:308–315
5. Georgakilas V, Tiwari JN, Kemp KC, Perman JA, Bourlinos AB, Kim KS, Zboril R (2016) Noncovalent functionalization of graphene and graphene oxide for energy materials, biosensing, catalytic, and biomedical applications. Chem Rev 116:5464–5519
6. Rodrigo D, Limaj O, Janner D, Etezadi D, García de Abajo FJ, Pruneri V, Altug H (2015) Mid-infrared plasmonic biosensing with graphene. Science 349:165–168
7. Morales-Narváez E, Merkoçi A (2012) Graphene oxide as an optical biosensing platform. Adv Mater 24:3298–3308
8. Chiu N-F, Huang T-Y, Kuo C-C, Lee W-C, Hsieh M-H, Lai H-C (2012) Single-layer graphene based SPR biochips for tuberculosis bacillus detection. Proc SPIE 8427:84273M–842737M
9. Chiu N-F, Huang T-Y (2014) Sensitivity and kinetic analysis of graphene oxide-based surface plasmon resonance biosensors. Sensors Actuators B Chem 197:35–42
10. Zhang H, Sun Y, Gao S, Zhang J, Zhang H, Song D (2013) A novel graphene oxide-based surface plasmon resonance biosensor for immunoassay. Small 9:2537–2540
11. Stebunov YV, Aftenieva OA, Arsenin AV, Volkov VS (2015) Highly sensitive and selective sensor chips with graphene-oxide linking layer. ACS Appl Mater Interfaces 7:21727–21734
12. Allen MJ, Tung VC, Kaner RB (2010) Honeycomb carbon: A review of graphene. Chem Rev 110:132–145
13. Novoselov KS, Geim AK, Morozov SV, Jiang D, Zhang Y, Dubonos SV, Grigorieva IV, Firsov AA (2004) Electric field effect in atomically thin carbon films. Science 306:666–669
14. Kim KS, Zhao Y, Jang H, Lee SY, Kim JM, Kim KS, Ahn J-H, Kim P, Choi J-Y, Hong BH (2009) Large-scale pattern growth of graphene films for stretchable transparent electrodes. Nature 457:706–710
15. Wang K, Ruan J, Song H, Zhang J, Wo Y, Guo S, Cui D (2011) Biocompatibility of graphene oxide. Nanoscale Res Lett 6:8–15
16. Liu Y, Yu D, Zeng C, Miao Z, Dai L (2010) Biocompatible graphene oxide-based glucose biosensors. Langmuir 26:6158–6160
17. Shao Y, Wang J, Wu H, Liu J, Aksay IA, Lin Y (2010) Graphene based electrochemical sensors and biosensors: A Review. Electroanalysis 22:1027–1036
18. Chen K, Zhang Z-L, Liang Y-M, Liu W (2013) A graphene-based electrochemical sensor for rapid determination of phenols in water. Sensors 13:6204–6216

Chiu *et al. Nanoscale Research Letters* (2018) 13:152

Page 10 of 11

19. Chiu N-F, Huang T-Y, Lai H-C, Liu K-C (2014) Graphene oxide-based SPR biosensor chip for immunoassay applications. Nanoscale Res Lett 9:445–451

20. Chiu N-F, Fan S-Y, Yang C-D, Huang T-Y (2017) Carboxyl-functionalized graphene oxide composites as SPR biosensors with enhanced sensitivity for immunoaffinity detection. Biosens Bioelectron 89:445–450

21. Chiu N-F, Kuo C-T, Lin T-L, Chang C-C, Chen C-Y (2017) Ultra-high sensitivity of the non-immunological affinity of graphene oxide-peptide-based surface plasmon resonance biosensors to detect human chorionic gonadotropin. Biosens Bioelectron 94:351–357

22. Bao Q, Loh KP (2012) Graphene photonics, plasmonics, and broadband optoelectronic devices. ACS Nano 6:3677–3694

23. Luo Z, Vora PM, Mele EJ, Charlie Johnson AT, Kikkawa JM (2009) Photoluminescence and band gap modulation in graphene oxide. Appl Phys Lett 94:111909

24. Thomas HR, Vallés C, Young RJ, Kinloch IA, Wilson NR, Rourke JP (2013) Identifying the fluorescence of graphene oxide. J Mater Chem C 1:338–342

25. Zhang J, Sun Y, Wu Q, Gao Y, Zhang H, Bai Y, Song D (2014) Preparation of graphene oxide-based surface plasmon resonance biosensor with Au bipyramid nanoparticles as sensitivity enhancer. Colloids Surf B Biointerfaces 116:211–218

26. Nayak JK, Parhi P, Jha R (2015) Graphene oxide encapsulated gold nanoparticle based stable fibre optic sucrose sensor. Sensors Actuators B Chem 221:835–841

27. Zhang D, Huarng MC, Alocilja EC (2010) A multiplex nanoparticle-based bio-barcoded DNA sensor for the simultaneous detection of multiple pathogens. Biosens Bioelectron 26:1736–1742

28. Wang Y, Alocilja EC (2015) Gold nanoparticle-labeled biosensor for rapid and sensitive detection of bacterial pathogens. J Biol Eng 9:16–22

29. Rai VN, Srivastava AK, Mukherjee C, Deb SK (2012) Surface enhanced absorption and transmission from dye coated gold nanoparticles in thin films. Appl Opt 51:2606–2615

30. Ahmed S, Ahmad M, Swami BL, Ikram S (2016) A review on plants extract mediated synthesis of silver nanoparticles for antimicrobial applications: A green expertise. J Adv Res 7:17–28

31. Gu X, Qiu T, Zhang W, Chu PK (2011) Light-emitting diodes enhanced by localized surface plasmon resonance. Nanoscale Res Lett 6:199–210

32. Khan AK, Rashid R, Murtaza G, Zahra A (2014) Gold nanoparticles: synthesis and applications in drug delivery. Trop J Pharm Res 13:1169–1177

33. Dhand C, Dwivedi N, Loh XJ, Ying ANJ, Verma NK, Beuerman RW, Lakshminarayanan R, Ramakrishna S (2015) Methods and strategies for the synthesis of diverse nanoparticles and their applications: a comprehensive overview. RSC Adv 5:105003–105037

34. Zhang X (2015) Gold nanoparticles: recent advances in the biomedical applications. Cell Biochem Biophys 72:771–775

35. Nune SK, Gunda P, Thallapally PK, Lin Y-Y, Forrest ML, Berkland CJ (2009) Nanoparticles for biomedical imaging. Expert Opin Drug Deliv 6:1175–1194

36. Huang X, El-Sayed MA (2010) A hybrid system with highly enhanced graphene SERS for rapid and tag-free tumor cells detection. J Adv Res 1:13–28

37. Hwang S, Nam J, Jung S, Song J, Doh H, Kim S (2014) Gold nanoparticle-mediated photothermal therapy: current status and future perspective. Nanomedicine 9:2003–2022

38. Kang S, Lee J, Ryu S, Kwon Y, Kim K-H, Jeong DH, Paik SR, Kim B-S (2017) Gold nanoparticle/graphene oxide hybrid sheets attached on mesenchymal stem cells for effective photothermal cancer therapy. Chem Mater 29:3461–3476

39. Cormode DP, Naha PC, Fayad ZA (2014) Nanoparticle contrast agents for computed tomography: a focus on micelles. Contrast Media Mol Imaging 9:37–52

40. Jain S, Hirst DG, O'Sullivan JM (2012) Gold nanoparticles as novel agents for cancer therapy. Br J Radiol 85:101–113

41. Saha K, Agasti SS, Kim C, Li X, Rotello VM (2012) Gold nanoparticles in chemical and biological sensing. Chem Rev 112:2739–2779

42. Li YY, Schluesener HJ, Xu SQ (2010) Gold nanoparticle-based biosensors. Gold Bull 43:29–41

43. Khalil I, Julkapli NM, Yehye WA, Basirun WJ, Bhargava SK (2016) Graphene–gold nanoparticles hybrid—synthesis, functionalization, and application in a electrochemical and surface-enhanced raman scattering biosensor. Materials 9:406–443

44. Niemeyer CM (2001) Nanoparticles, proteins, and nucleic acids: biotechnology meets materials science. Angew Chem Int Ed 40:4128–4158

45. Wang Z, Ma L (2009) Gold nanoparticle probes. Coord Chem Rev 253:1607–1618

46. Ma L-N, Liu D-J, Wang Z-X (2010) Synthesis and applications of gold nanoparticle probes. Chin J Anal Chem 38:1–7

47. Yu P, Yao Y, Wu J, Niu X, Rogach AL, Wang Z (2017) Effects of plasmonic metal core -dielectric shell nanoparticles on the broadband light absorption enhancement in thin film solar cells. Sci Rep 7:7696

48. Wu J, Yu P, Susha AS, Sablon KA, Chen H, Zhou Z, Li H, Ji H, Niu X, Govorov AO, Rogach AL, Wang ZM (2015) Broadband efficiency enhancement in quantum dot solar cells coupled with multispiked plasmonic nanostars. Nano Energy 13:827–835

49. Abideen I, Gbadebo Y, Abass F (2017) Substrate temperature effect on the photophysical and microstructural properties of fluorine-doped tin oxide nanoparticles. J Semicond 38:072001

50. Zhan L, Li CM, Wu WB, Huang CZ (2014) A colorimetric immunoassay for respiratory syncytial virus detection based on gold nanoparticles–graphene oxide hybrids with mercury-enhanced peroxidase-like activity. Chem Commun 50:11526–11528

51. Hu L, Yuan Y, Zhang L, Zhao J, Majeed S, Xu G (2013) Copper nanoclusters as peroxidase mimetics and their applications to H2O2 and glucose detection. Anal Chim Acta 762:83–86

52. Wang Q, Li Q, Yang X, Wang K, Du S, Zhang H, Nie Y (2016) Graphene oxide–gold nanoparticles hybrids-based surface plasmon resonance for sensitive detection of microRNA. Biosens Bioelectron 77:1001–1007

53. Choi Y, Bae HS, Seo E, Jang S, Park KH, Kim B-S (2011) Hybrid gold nanoparticle-reduced graphene oxide nanosheets as active catalysts for highly efficient reduction of nitroarenes. J Mater Chem 21:15431

54. Saeed AA, Sánchez JLA, O'Sullivan CK, Abbas MN (2017) DNA biosensors based on gold nanoparticles-modified graphene oxide for the detection of breast cancer biomarkers for early diagnosis. Bioelectrochemistry 118:91–99

55. Wu L, Lu X, Fu X, Wu L, Liu H (2017) Gold nanoparticles dotted reduction graphene oxide nanocomposite based electrochemical aptasensor for selective, rapid, sensitive and congener-specific PCB77 detection. Sci Rep 7:5191

56. Hernández-Sánchez D, Villabona-Leal G, Saucedo-Orozco I, Bracamonte V, Pérez E, Bittencourtd C, Quintana M (2018) Stable graphene oxide–gold nanoparticle platforms for biosensing applications. Phys Chem Chem Phys 20:1685–1692

57. Zhang B, Cui Y, Chen H, Liu B, Chen G, Tang D (2011) A new electrochemical biosensor for determination of hydrogen peroxide in food based on well-dispersive gold nanoparticles on graphene oxide. Electroanalysis 23:1821–1829

58. Hong W, Bai H, Xu Y, Yao Z, Gu Z, Shi G (2010) Preparation of gold nanoparticle/graphene composites with controlled weight contents and their application in biosensors. J Phys Chem C 114:1822–1826

59. Khalil I, Julkapli NM, Yehye WA, Basirun WJ, Bhargava SK (2016) A hybrid system with highly enhanced graphene SERS for rapid and tag-free tumor cells detection. Materials 9:406–444

60. Hummers WS, Offeman RE (1958) Preparation of graphitic oxide. J Am Chem Soc 80:1339–1339

61. Chang C-C, Chen C-P, Lee C-H, Chen C-Y, Lin C-W (2014) Colorimetric detection of human chorionic gonadotropin using catalytic gold nanoparticles and a peptide aptamer. Chem Commun 50:14443

62. Jin Q, Xu J-P, Ji J, Shen J-C (2008) Zwitterionic phosphorylcholine as a better ligand for stabilizing large biocompatible gold nanoparticles. Chem Commun 0:3058–3060

63. Link S, El-Sayed MA, Phys J (1999) Size and Temperature Dependence of the Plasmon Absorption of Colloidal Gold Nanoparticles. Chem B 103:4212–4217

64. Young JK, Lewinski NA, Langsner RJ, Kennedy LC, Satyanarayan A, Nammalvar V, Lin AY, Drezek RA (2011) Size and Temperature Dependence of the Plasmon Absorption of Colloidal Gold Nanoparticles. Nanoscale Res Lett 6:428–438

65. su Y-J, Hung Y-J, Lin Y-C, Lai Y-L, Chang H-T, Wang C-H, Chan YL, Hsia C-L, Luo M-F, Lee C-H, Wei DH (2011) The origin of interfacial electronic and magnetic degradation for a ferromagnet atop organic conjugated molecules. Syn Metals 161:575–580

66. Acik M, Lee G, Mattev C, Chhowalla M, Cho K, Chabal YJ (2010) Unusual infrared-absorption mechanism in thermally reduced graphene oxide. Nat Mater 9:840–845

67. Singh S, Tuteja SK, Sillu D, Deep A, Suri CR (2016) Gold nanoparticles-reduced graphene oxide based electrochemical immunosensor for the cardiac biomarker myoglobin. Microchim Acta 183:1729–1738

Chiu *et al. Nanoscale Research Letters* (2018) 13:152

Page 11 of 11

68. Chuang M-K, Lin S-W, Chen F-C, Chu C-W, Hsu C-S (2014) Gold nanoparticle-decorated graphene oxides for plasmonic-enhanced polymer photovoltaic devices. Nanoscale 6:1573–1579
69. Jamil AKM, Izake EL, Sivanesan A, Fredericks PM (2015) Rapid detection of TNT in aqueous media by selective label free surface enhanced Raman spectroscopy. Talanta 134:732–738
70. Shen J, Shi M, Yan B, Ma H, Li N, Hu Y, Ye M (2010) Covalent attaching protein to graphene oxide via diimide-activated amidation. Colloids Surf B Biointerfaces 81:434–438
71. Zhang W, Cui J, Tao CA, Wu Y, Li Z, Ma L, Wen Y, Li G (2009) A strategy for producing pure single-layer graphene sheets based on a confined self-assembly approach. Angew Chem Int Ed 48:5864–5868